

New tomographic approach for deconvolution of ion velocity and temperature profiles in a plasma centrifuge

N P Poluektov and N P Efremov

Department of Physics, Faculty of Electronics, Moscow State University of Forestry,
141001 Mytischki-1, Moscow Region, Russia

Received 14 October 1997, in final form 23 January 1998

Abstract. Tomographic equations for the velocity and temperature of heavy particles in plasma have been derived using the relations of the velocity distributions with the Doppler shift and broadening of the spectral lines. These equations are correct for non-Maxwellian velocity distributions and for arbitrary plasma flow. This approach was used for the computation of ion velocity and temperature radial distributions from the spectroscopic data in a highly ionized plasma centrifuge. Separation factors of 15 for Ar–Kr and 22 for Ar–Xe mixtures with a density of 10^{-21} m^{-3} are obtained.

1. Introduction

Plasma centrifuges have been intensively investigated for use in element and isotope separation [1, 2]. Significant levels of isotope enrichment have been reported in so-called vacuum-arc centrifuges [3, 4]. It was found that the rotation frequency in these devices increases linearly with magnetic field B , but the radial size of the plasma column decreases with B . The measured Gaussian density profile implies that the bulk of the plasma is in the core of the column, where the enrichment is weakest. This leads to a limitation of the output of enriched isotopes in this centrifuge. To maximize the enrichment, it is better to produce a hollow column, with most of the plasma off the axis.

In this paper we describe an experimental study of a highly ionized pulsed plasma centrifuge with off-axis density. Discharge parameters are: current $I < 7 \text{ kA}$, initial pressure $p_0 = 1.33\text{--}13.3 \text{ Pa}$, power $0.1\text{--}5 \text{ MW}$, pulse length 3 ms , magnetic field $B_0 < 0.7 \text{ T}$, plasma density $n \approx 10^{21} \text{ m}^{-3}$, velocity of the rotation $V_\theta = (5\text{--}25) \times 10^3 \text{ m s}^{-1}$, ion temperature $T_i = 5\text{--}25 \text{ eV}$. We present the first results of the ion velocity and temperature radial distributions. These distributions were calculated from spectroscopic measurements using velocity and temperature tomography equations, taken from [5].

The determination of the ion velocity and temperature profile in the core of a highly ionized rotating plasma is a most complex problem, for the following reasons. In a highly ionized plasma the probe measurements are limited by the boundary layers. Laser induced fluorescence

(LIF) and charge exchange recombination methods [6] are expensive and time consuming for pulse discharges, therefore they are seldom used. In the spectroscopy method based on the Doppler shift and broadening of the spectral line respectively, the profile obtained is integrated along the direction of observation. The tomographic approach must then be used in order to obtain the spatial dependence. Up to now the tomography equation has been used only to inverse the emission of radiation ε . Ion temperature profile deconvolution is therefore a complex procedure [7].

The problem of velocity and temperature reconstruction has been solved only for particular cases of an axial flow and/or a small monotonic temperature variation [8]. The problem is more complicated in the case of a rotating plasma, where the velocity and temperature profiles are usually humped and have a large radial gradient. The line integrated measurement of the spectral line profile would include both directed and random energy components and thus may lead to the conclusion that the ion temperature is higher than the actual one. The local emission coefficient $\varepsilon(v, r, \eta)$ depends on the direction of observation η due to the Doppler effect and therefore the inversion of each frequency is not possible.

We also measured the separation factor α for various gas mixtures using a mass spectrometer. The value of α agrees with the spectral measurements of velocity and temperature distributions. It is significant that a large separation factor is obtained in the area where plasma density is a maximum.

2. Experimental apparatus

Figure 1 shows schematically the plasma centrifuge apparatus. The stainless steel vacuum vessel has a diameter of 0.3 m and is 1.2 m long. Inside the chamber are two molybdenum cathode rods ($r = 1.5$ cm, $l = 8$ cm) and anode rings ($r = 7.5$ cm) connected to the chamber and two quartz or nitride-boron insulators ($r = 5$ cm) at a distance of 0.55 m from each other. Four coils produce a mirror-like magnetic field with a decay time of 10 ms. The magnetic field strength is $B_0 < 0.7$ T in a midplane and three times greater near the insulator. The direction of the current in the magnetic coils can be changed as required for clockwise or counterclockwise plasma rotation. The magnetic field lines can be assumed to be equipotential (plasma potential $\varphi_p = \text{constant}$) due to a high conductivity of the plasma along B . Thus the magnetic field lines touching the cathode and anode rings form 'plasma electrodes' [9]. A highly ionized rotating plasma is created in the volume bounding the plasma electrodes and insulator endplates. An azimuthal plasma velocity V_θ at first approximation is equal to $V_\theta = E_r/B_z$, where $E_r = -d\varphi/dr$. With equipotential magnetic field lines the angular plasma velocity is constant along B (the isorotation law [9]). The initial pressure is 1.33–13.3 Pa. In a maximum of the magnetic field the gas in the chamber is ionized by supplying power from the capacitor bank C_1 (400 μF , $U_1 = 10$ kV). The second capacitor bank C_2 (2000 μF , $U_2 = 5$ kV) is connected at time t_2 through the inductance L for further acceleration of the plasma.

The radial velocity distribution near the endplate insulator was obtained by measuring the floating potential φ_f by means of eight radially mounted probes. The difference between the gradient of plasma and floating potentials is small because the electron temperature of 2–4 eV is weakly changed in space. The probes were made of tungsten, having a height of 2 mm and a radius of 0.17 mm and not being disturbed by the plasma rotation. Using a time-of-flight mass spectrometer the separation factor was measured

$$\alpha = \frac{n_2(r_2)}{n_1(r_2)} : \frac{n_2(r_1)}{n_1(r_1)} \quad (1)$$

where n_1 and n_2 denote the density of any two species considered and r is the radial distance from the axis. A fast-acting valve was used to extract a sample of gas from a plasma at a particular time of discharge and subsequently the sample was analysed with a mass spectrometer. The construction of a sample probe is similar to the method described earlier [10]. The sampling time is 0.4 ms.

The rotating velocity V_θ and the ion temperatures T_i were measured by a spectral method from emission line profiles. For heavy particles (Ar, Kr, Xe) the Stark broadening is small in comparison with the Doppler broadening and can be ignored. The Zeeman broadening was isolated by means of a polaroid. We used 4806 \AA $\text{Ar}^+(4s^4 P_{5/2} - 4p^4 P_{5/2})$ and 5292 \AA $\text{Xe}^+(4s^4 P_{5/2} - 6p^4 P_{5/2})$, splitting in a magnetic field into one π and two σ components. A schematic view of the optical system is shown in figure 2. Light from the chord

in the midplane is focused into a 2.6 m spectrometer (grating 2400 mm^{-1} , dispersion 1.5 $\text{\AA} \text{mm}^{-1}$) and into a spectrometer B (grating 1200 mm^{-1} , dispersion 6 $\text{\AA} \text{mm}^{-1}$). The line of sight along 12–15 chords was scanned shot-by-shot by moving the mirror. By means of a dissector with a $0.05 \times 12 \text{ mm}^2$ slit behind the spectrometer the line profile was measured eight times during the discharge (scan time 10–30 μs , period 25–100 μs). The instrumental function of spectrometer A and a dissector with a full width at half-maximum (FWHM) of 0.05 \AA was found by means of He–Ne and Cd lasers. The emission intensity necessary to reconstruct the velocity and temperature was at first determined by integration of the emission signal over the entire profile, measured by the dissector. This method in some cases results in inadequate reconstruction of the velocity and temperature because of the low signal-to-noise ratio of the dissector. Then the line intensity was detected by a photomultiplier at spectrometer B with a large entrance slit width, which increased the signal-to-noise ratio and raised the precision of the emission, velocity and (mainly) temperature reduction (the emission cones detected by spectrometers A and B are equal). The reproducibility of the radiation shot-by-shot was monitored with the photomultiplier mounted on a monochromator, which measured the line intensity along the chamber. The electron density n_e was calculated from the Stark broadening of the H_β line (5% of hydrogen was added to the discharge).

The signal from each chord was averaged by three to four shots for both clockwise and counterclockwise plasma rotation. A computer system was used to acquire the data. The data acquisition system based on computer application to measurement and control (CAMAC) apparatus consists of (figure 2) a synchronizer, a digital-to-analogue converter, a paraphased amplifier (± 400 V) for deflected plates of the dissector, and three 8-bit analogue-to-digital converters (20 MHz, 1 kByte buffer memory). The line profile consists of 64–256 sampling points of the analogue-to-digital converter. In addition two digital two-channel oscilloscopes are used to measure the discharge current (by the Rogowski coils) and the voltage.

The observed line profile gives an average value along the chord. The radial profiles of temperature and velocity were then calculated using the tomographic equations of velocity and temperature, derived by the authors [5].

3. The tomographic equations of heavy-particle velocity and temperature in plasma

As mentioned above, the tomographic approach must be used in order to obtain the radial profile of heavy-particle velocity and temperature. The two-dimensional Radon transformation for the spectral intensity $I(v, p, \xi)$ along the line of observation is given by [11]

$$I(v, p, \xi) = \hat{R}\varepsilon(v, r, \eta) = \int \varepsilon(v, r, \eta) \delta(p - \xi r) d^2 r \quad (2)$$

where r is the radius vector, η, ξ are vectors along and

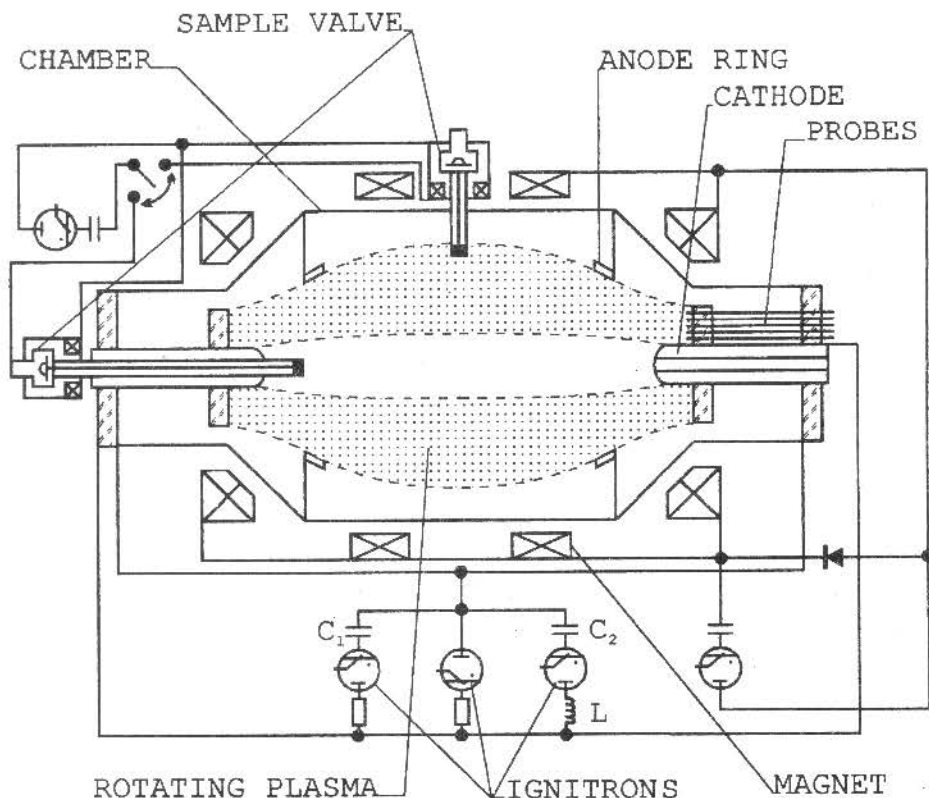


Figure 1. Schematic diagram of the plasma centrifuge apparatus.

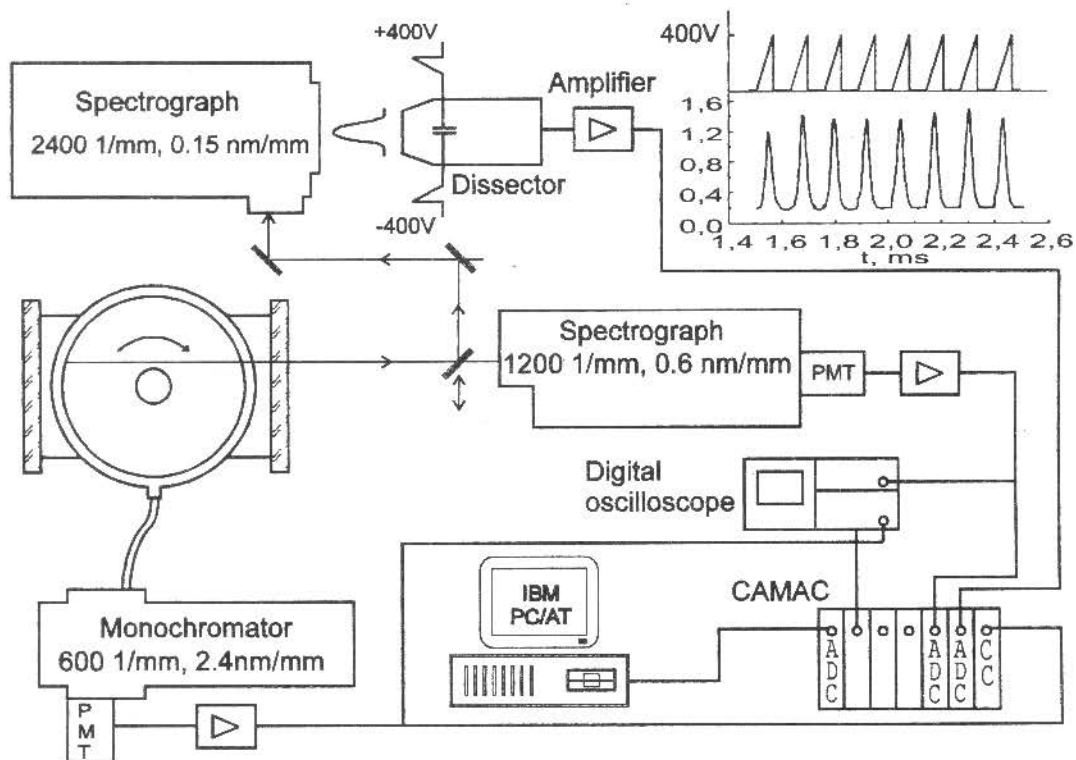


Figure 2. The set-up of the optical diagnostic.

perpendicular to the direction of observation, p is the distance to the observation line, $\delta(p - \xi r)$ is the Dirac delta function and \hat{R} is an operator for the Radon transform. We

emphasize that $\varepsilon(v, r, \eta)$ is an anisotropic value due to the Doppler effect and therefore the inversion of equation (2) on each frequency is not possible.

We first derive the tomographic equations for the velocity and temperature. We consider an optically thin plasma emitting spectral lines and assume that the linewidth profile is predominantly caused by the Doppler effect (in the general case of a non-Maxwellian distribution the shape of the line is not the Gaussian profile). Then the velocity distribution of the atoms $\rho(V)$ is related to the normalized distribution of the emitted radiation $g(v)$ in the required direction, namely

$$\rho(V) dV = g(v) dv = \frac{\varepsilon(v, \mathbf{r}) dv}{\int_0^\infty \varepsilon(v, \mathbf{r}) dv} \quad (3)$$

$$V = \frac{c}{v_0}(v - v_0) \quad (4)$$

where v, v_0 are the Doppler shifted and unshifted frequencies respectively, c is the speed of light and $\varepsilon(v, \mathbf{r})$ is the local spectral emission coefficient.

In the thermodynamic the mean velocity and temperature are given by the formulae

$$\langle V \rangle = \int_{-\infty}^{\infty} V \rho(V) dV \quad (5)$$

$$\langle T \rangle = \frac{m}{2} \int_{-\infty}^{+\infty} (V - \langle V \rangle)^2 \rho(V) dV. \quad (6)$$

We will use formulae (5) and (6) to determine the heavy-particle temperature in plasma in the general non-local thermodynamic equilibrium case. Substituting equations (3) and (4) into equations (5) and (6), we get the equations for the mean particle velocity and temperature along the beam of observation:

$$\langle V \rangle \equiv V_\eta = \int_0^\infty g(v) \frac{c}{v_0} (v - v_0) dv \quad (7)$$

$$\langle T \rangle = \frac{mc^2}{2v_0^2} \left[\int_0^\infty (v - v_0)^2 g(v) dv - \left(\int_0^\infty (v - v_0) g(v) dv \right)^2 \right]. \quad (8)$$

Multiplying equation (2) by $c(v - v_0)/v_0$ and $mc^2(v - v_0)^2/2v_0^2$, integrating over v , and using (3)–(8), we get the tomographic equations of the velocity and temperature respectively:

$$F(p, \xi) = \frac{c}{v_0} \int_0^\infty (v - v_0) I(v, p, \xi) dv = \int_{\infty} \varepsilon_0(\mathbf{r}) (\mathbf{V}(\mathbf{r}) \cdot \boldsymbol{\eta}) \delta(p - \xi \mathbf{r}) d^2 r \quad (9)$$

$$Z(p, \xi) = \frac{mc^2}{2v_0^2} \int_0^\infty (v - v_0)^2 I(v, p, \xi) dv = \int \varepsilon_0(\mathbf{r}) \left[T(\mathbf{r}) + \frac{mV_\eta^2(\mathbf{r})}{2} \right] \delta(p - \xi \mathbf{r}) d^2 r \quad (10)$$

where $\varepsilon_0(\mathbf{r}) = \int_0^\infty \varepsilon(v, \mathbf{r}, \boldsymbol{\eta}) dv$ is the integral emission coefficient, which does not depend on the direction of observation. To invert the velocity and temperature of a heavy particle it is necessary also to use the tomographic equation for the emission ε_0 :

$$\varphi(p, \xi) = \int_0^\infty I(v, p, \xi) dv = \int_{\infty} \varepsilon_0(\mathbf{r}) \delta(p - \xi \mathbf{r}) d^2 r. \quad (11)$$

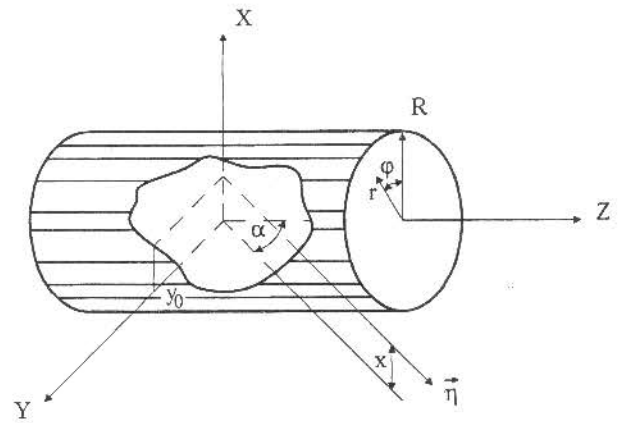


Figure 3. Observation scheme for a cylindrical plasma.

This equation has been studied in detail and the methods for its solution are known [12].

These equations are correct for non-Maxwellian velocity distributions and for arbitrary plasma flow. The calculation of spatial dependences of the velocity and the temperature from these formulae is based on an integration procedure. This makes possible processing of data having large noise unlike the determination of the shift and of the half-width from the first and second derivative respectively of the line profile. In an axisymmetrical plasma flow using the formulae of the vector analysis, the following formula for V_η can be obtained:

$$V_\eta = x \left(\frac{V_\theta}{r} \sin \alpha \right) + y \left(\frac{V_r}{r} \sin \alpha \right) + V_z \cos \alpha \quad (12)$$

where the notations are clear from figure 3. Substituting equation (12) in equations (9)–(11) we get

$$\varphi(x) = \frac{2}{|\sin \alpha|} \int_x^R \frac{\varepsilon_0(r) r dr}{(r^2 - x^2)^{1/2}} \quad (13)$$

$$F(x, \alpha) = 2 \operatorname{sign}(\sin \alpha) \int_x^R (x V_\theta + r V_z \operatorname{ctg} \alpha) \frac{\varepsilon_0(r) dr}{(r^2 - x^2)^{1/2}} \quad (14)$$

$$Z(x, \alpha) = \frac{2}{|\sin \alpha|} \int_x^R \frac{\varepsilon_0(r) r dr}{(r^2 - x^2)^{1/2}} \left[T(r) + \frac{(r^2 - x^2)}{r^2} \times \frac{mV_r^2}{2} \sin^2 \alpha + \frac{m}{2} \left(\frac{x}{r} V_\theta \sin \alpha + V_z \cos \alpha \right)^2 \right]. \quad (15)$$

For the observation angle $\alpha = \pi/2$, equations (13)–(15) become

$$\varphi(x) = \int_0^\infty I(v, x) dv = 2 \int_x^R \frac{\varepsilon_0(r) r dr}{(r^2 - x^2)^{1/2}} \quad (16)$$

$$F(x) = \frac{c}{v_0} \int_0^\infty (v - v_0) I(v, x) dv = 2 \int_x^R \frac{\varepsilon_0(r) V_\theta(r) x dr}{(r^2 - x^2)^{1/2}} \quad (17)$$

$$Z(x) = \frac{mc^2}{2v_0^2} \int_0^\infty (v - v_0)^2 I(v, x) dv = 2 \int_x^R \frac{\varepsilon_0(r) r dr}{(r^2 - x^2)^{1/2}} \left[T(r) + \frac{mV_\theta^2}{2} \left(\frac{x}{r} \right)^2 \right]. \quad (18)$$

In equation (18) it is suggested that $mV_r^2/2 \ll T$ and $|V_r/V_\theta| \ll 1$. The second term in the square brackets

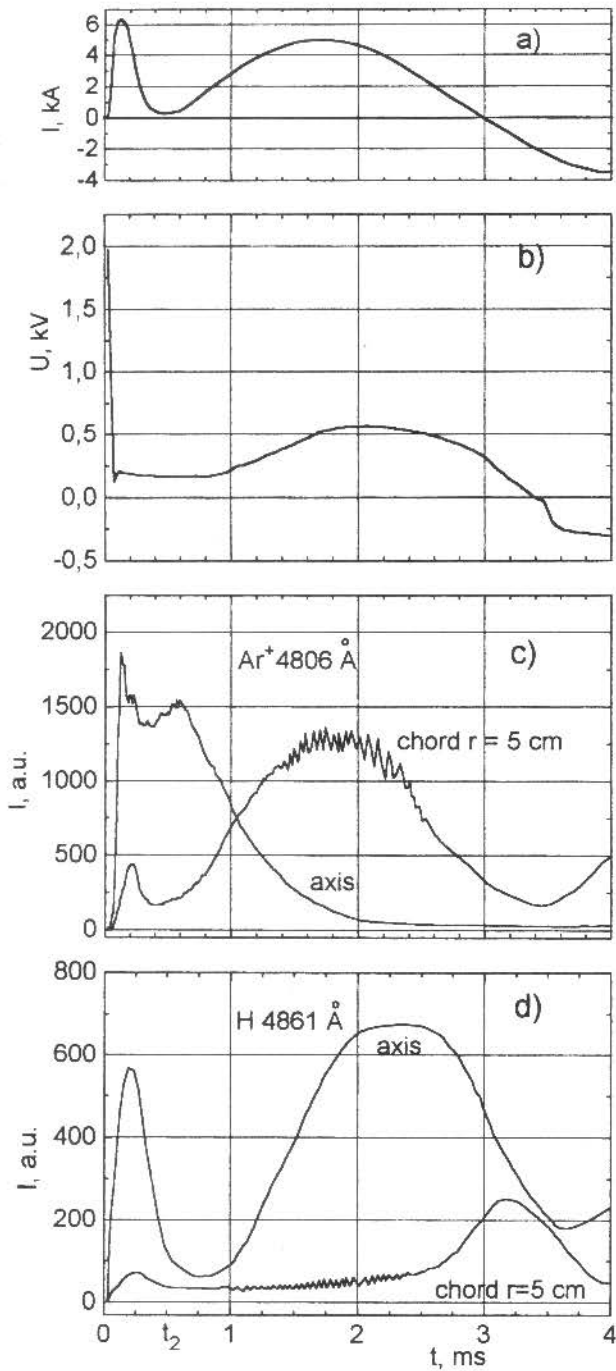


Figure 4. Time dependence of discharge current (a), voltage (b), the Ar^+ 4806 Å emission (c) and the H 4861 Å emission (d). 70% Ar + 30% H_2 mixture, $p_0 = 7$ Pa, $B_0 = 0.6$ T, $U_2 = 4$ kV.

in (18) is the contribution of macroscopic motion to the line broadening.

The integral equations (16)–(18) have been solved numerically in matrix form using the Tikhonov regularization method [12]. The solution of the matrix equation $A\varphi = f$ is given $\varphi = A^T f / (A^T A + \alpha\Omega)$, where A^T , Ω are the transposed and regularized matrices respectively and α is the coefficient of the regularization. The reconstruction procedure is as follows: first, the emission ε_0 is inverted from equation (16), then the velocity from equation (17)

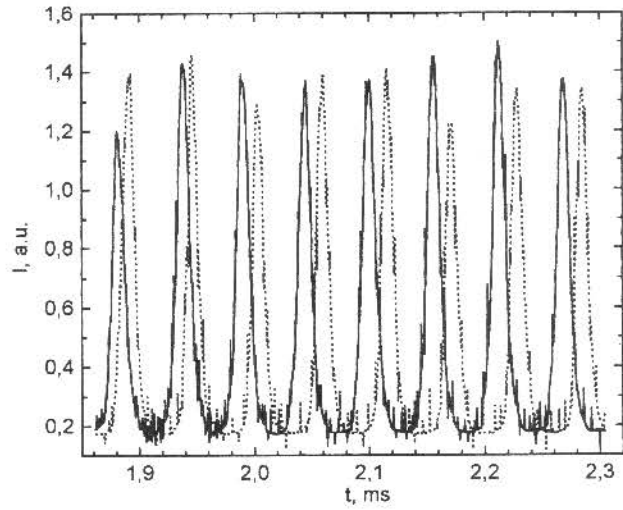


Figure 5. Two sets of the Ar^+ 4806 Å profiles obtained by a dissector along the chord $r = 6$ cm in two shots with opposite directions of rotation. Ar , $p_0 = 7$ Pa, $B_0 = 0.5$ T, $U_2 = 4$ kV.

and finally the temperature from equation (18). Noteworthy features of this rotating plasma are the hollow density and velocity profiles and great (up to -30%) fluctuations of the radiation, that complicate the inversion solution. The reconstruction errors of the latter parameters depend on the inversion errors of the former, therefore the spectrometer B was used to increase the inversion accuracy of the temperature.

4. Experimental results and discussion

Figures 4(a) and (b) show the typical current and voltage of the discharge. The current from the bank C_2 has a sinusoidal form and at time 3 ms is reversed and the plasma rotates in the opposite direction. We shall not consider this opposite rotation period further. The electron density, measured by broadening of the H_β line, increases in time up to 0.3 ms and then becomes roughly constant. The value of $n_e = 5 \times 10^{21} \text{ m}^{-3}$ (mean along the chord at $r = 7$ cm) is achieved at $p_0 = 13.3$ Pa and $B_0 = 0.7$ T. The plasma density increases nearly in proportion to magnetic field strength, discharge current and initial pressure. The electron density measured along the axis of the chamber through the channel in the cathode is ten times less. This large radial density enhancement is because of a centrifugal force. Figures 4(c) and (d) show the emission intensities of the Ar^+ (4806 Å) and H_β (4861 Å) along the chamber axis and chord ($r = 5$ cm) in the discharge of the 70% Ar + 30% H_2 mixture. The strong centrifugal force moves the heavy ions to the outer wall, when plasma is accelerated, and therefore the emission of argon ions increases at the chord and drops at the axis. The picture is the direct opposite of what happens to light hydrogen atoms. Similar results were obtained in the Ar – He mixture. The emission intensity depends exponentially on the electron temperature, which may contribute to the time variation of the emission. The electron temperature T_e was measured from relative intensities of the ion and neutral Ar lines [13].

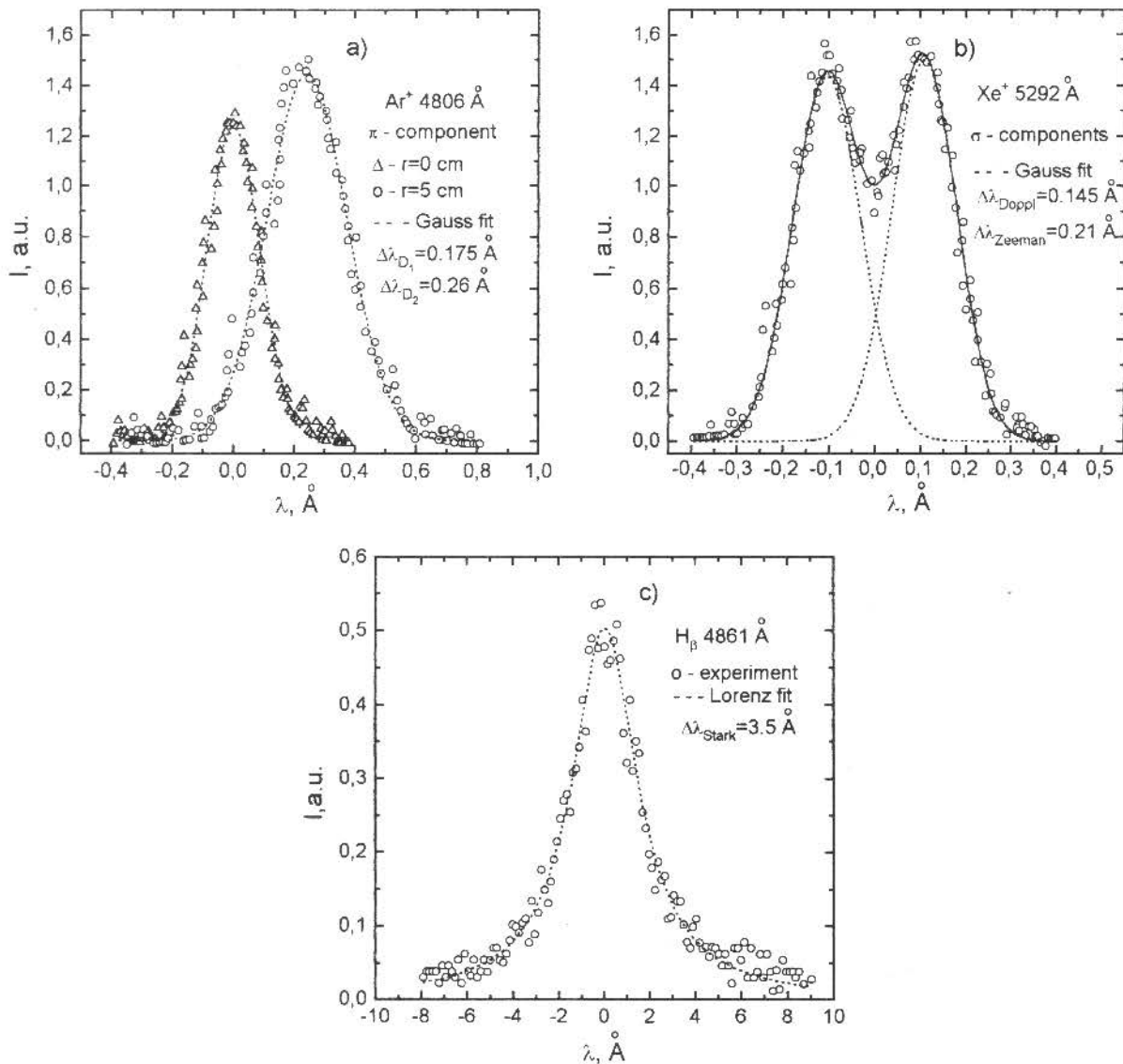


Figure 6. The line profiles of (a) Ar^+ 4806 \AA (π Zeeman component), (b) Xe^+ 5292 \AA ($\pm\sigma$ Zeeman components), (c) H_β 4861 \AA . \circ , Δ , the experimental shapes; ---, fitted with the Gaussian or the Lorentzian shapes. $p_0 = 6$ Pa, $B_0 = 0.6$ T, $U_2 = 4$ kV, $t = 1.8$ ms.

T_e can be determined with good accuracy from the line intensity ratios in the non-local thermodynamic equilibrium plasma if $\Delta E \gg kT_e$, where ΔE is the difference between excited energy levels (including ionization energy) and k is the Boltzmann constant. The electron temperature is equal to 2–4 eV in the range of plasma parameters studied and varies slightly in the time interval 1.5–2.5 ms.

Figure 5 shows two sets of the Ar^+ 4806 \AA profiles obtained along the chord $r = 6$ cm in two shots with an opposite direction of rotation.

Figure 6(a) shows the two profiles of the Ar^+ 4806 \AA line (π component), measured along the chords $r = 0$ and $r = 5$ cm respectively. The line at $r = 5$ cm is shifted and its linewidth is 1.6 times larger because of the macroscopic rotation. Figure 6(b) demonstrates the influence of the Zeemann effect on line shape. This contour was obtained along the diameter in a midplane of the chamber with a polarizer. The dotted curves in figures 6(a), (b) are the Gaussian fit to the measured profiles. Figure 6(c) shows

the line shape of the H_β 4861 \AA , obtained in experiment and the Lorentz fit, which was used to calculate plasma density.

Figure 7(a) shows the radial dependence of emission of argon ions and hydrogen atoms in an 80% Ar + 20% H mixture, obtained by Abel inversion. The profile of the Ar^+ emission is shifted to the major radius in comparison with the emission profile of hydrogen, which is the result of a separation process. The emission of neutral argon atoms after plasma acceleration is tens times less than that of ions, as a large outflux of neutral Ar gas occurs from the confinement area to the outer wall regions on account of elastic and charge-exchange collisions with rotating plasma ions. Notice that at the initial pressure $p_0 = 8$ –13.3 Pa plasma is composed predominantly of singly charged ions; at $p_0 \leq 7$ Pa the lines of two-charged ions arise in the emission. Figure 7(b) gives the radial distributions of the azimuthal velocity, obtained by Abel inversion (full curve) and by the integrated Doppler shift at various chords with

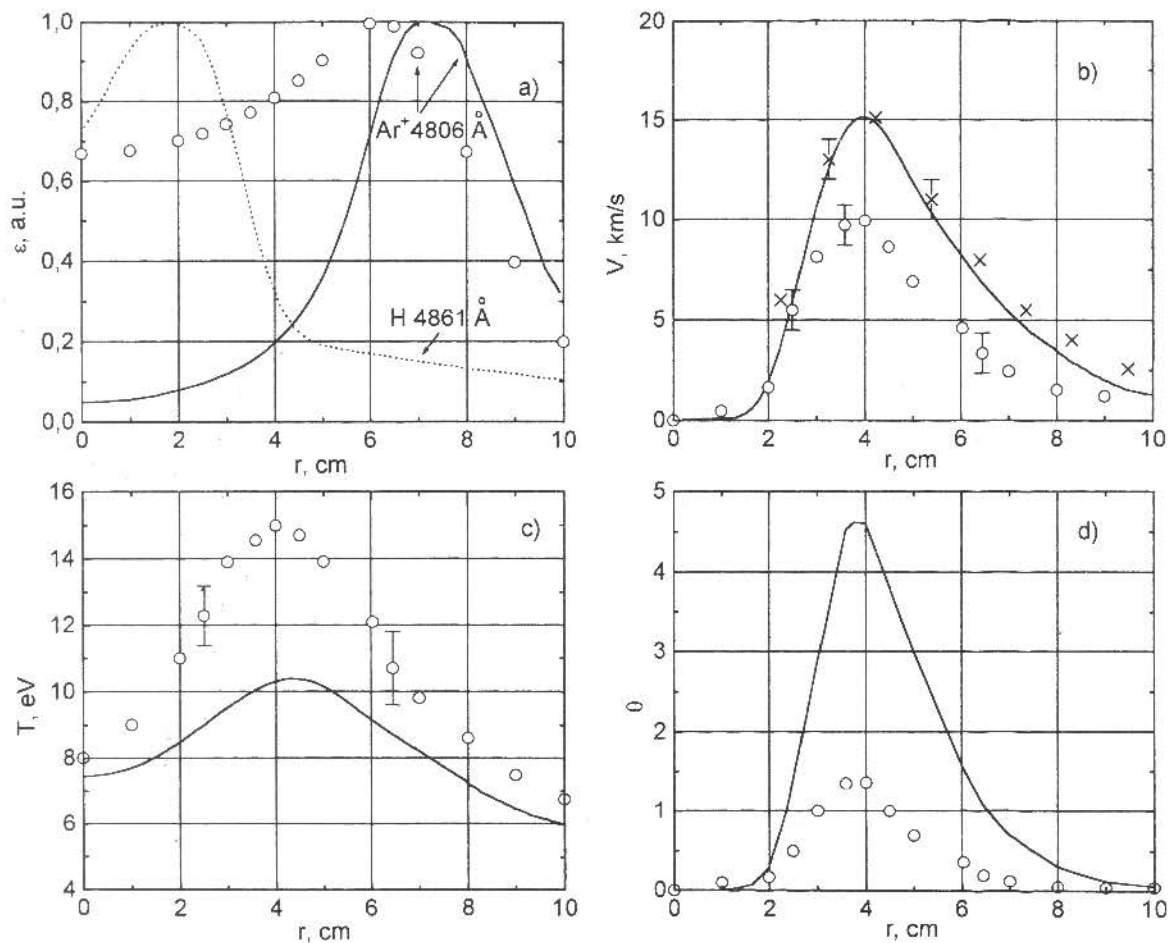


Figure 7. Radial distribution of (a) intensity of the emission, (b) ion velocity, (c) ion temperature, (d) $\theta = mV_i^2/2kT_i$. \circ , obtained from measurement along chords; —, Abel inversion (Ar^+ 4806 Å); ---, Abel inversion (H_β 4861 Å); \times , projected into a midplane by probe measurement near the insulator. 70% Ar + 30% H_2 mixture, $p_0 = 13.3$ Pa, $B_0 = 0.4$ T, $U_2 = 2$ kV, $t = 2$ ms.

the spectroscopic measurements (open circle). There is a great difference in these distributions, and without Abel-transformation the error can reach 100%. It is shown that the rotational velocity at the plasma cathode ($r = 2$ cm) and plasma anode ($r = 9$ cm) approaches zero. This figure also shows the radial velocity distribution, obtained with the probes near the insulator surface. This distribution is projected then into a midplane of the chamber using the isorotation law and the magnetic field line configuration, calculated with a computer. The radial profiles of the velocity obtained by the Abel inversion and by probe data are in good coincidence. The rotational velocity measurements (with probes and by spectroscopy) show that the velocity increases with increasing magnetic field and current and decrease of the pressure, but only up to a certain saturation level. The highest velocity near the insulator in a discharge with pure gas is equal to the critical velocity [14] within the limits of experimental error. For discharges in a gas mixture the situation is more complicated. The value of maximum velocity in this case depends on the gas mixture ratio and is in the range between critical velocities of gas components. The initial measurements by spectroscopy show that the velocities of various species of ions are different in the mixture discharge. This velocity mismatch

between different ions causes the azimuthal friction force, resulting in the separation. Work is continuing to determine how the velocity distribution in the mixture is affected by pressure, gas composition, magnetic field strength and power.

Figure 7(c) shows the radial distributions of the ion temperature, obtained from the Doppler broadening integrated along the chord and calculated from the inversion equation (18). These distributions differ considerably. The ion temperature profile has a maximum at $r = 4.5$ cm. This fact can be explained if it is assumed that the main ion heating mechanism is the viscous dissipation. The viscous heating term is equal to

$$P_\mu = \mu_\perp \left(r \frac{\partial}{\partial r} \frac{V_{\theta i}}{r} \right)^2.$$

Using μ_\perp for the transverse magnetic field viscosity, the expression given by Braginskii [15], $\mu_\perp = 0.3kT_i v_{ii}/\omega_i$, where v_{ii} denotes the ion-ion collision frequency and ω_i is the ion gyro frequency, we get a value of $m_\perp \approx 10^{-4}$ kg ms $^{-1}$. Then from the measured velocity profile and the value of μ_\perp obtained we can estimate of the magnitude of viscous heating $P_\mu = 1-10$ MW m $^{-3}$. For comparison we also calculate the magnitude of the Ohmic dissipation:

$Q = j_r^2/\sigma_{\perp}$, where j_r is the current density and σ_{\perp} the radial conductivity. The axial redistribution of the current takes place in a highly ionized rotating plasma. As a result the discharge current would tend to concentrate in the thin boundary layer close to the insulator (the Hartmann layer). The current density in the layer 0.5–1.5 cm from the insulator, measured by means of the sectional cathode [16] reaches 10^5 A m^{-2} and 10^4 A m^{-2} in the main plasma. If we assume that the radial current in a rotating plasma is fully carried by the ions and choose the value of $\sigma_{\perp} = 100 \Omega^{-1} \text{ m}^{-1}$, the Ohmic heating term is equal to about 10^2 MW m^{-3} in the boundary layer and 1 MW m^{-3} in the main plasma. Thus in a midplane the main heating mechanism is viscous dissipation. In the Hartmann layer Joule dissipation is more important.

Using the equation $j_r = n_e e \langle V_{ir} \rangle$ and measured electron and current densities we can calculate the mean value of radial ion velocity near the insulator: $\langle V_{ir} \rangle = 10^3\text{--}10^4 \text{ m s}^{-1}$ and 10^2 m s^{-1} in the midplane of the chamber. Thus the suggestions $mV_r^2/T_i \ll 1$ and $V_r/V_{\theta} \ll 1$, used in equation (18) are evaluated in a midplane.

From the measured velocity, temperature and plasma density one can evaluate the order of magnitude of different forces acting in a radial direction. The balance of the radial forces in a midplane is given by

$$\frac{\rho V_i^2}{r} = \frac{dp}{dr} - j_{\theta} B_z \quad (19)$$

where ρ is plasma mass density, p is the pressure and j_{θ} the azimuthal current density. The diamagnetic current I_{θ} arises from different azimuthal velocities of electrons and ions. The value of I_{θ} , measured by the Rogovski coil and magnetic probe, may be much as 10 kA [16]. The evaluation shows that the centrifugal force is essentially compensated by the Lorentz force $j_{\theta} B_z$ and in second order by the radial pressure gradient.

High rotational velocities and low heavy-particle temperatures are favourable for a good separation result. Therefore the relationship between the kinetic energy ($mV_i^2/2$) and the thermal energy (kT_i) (parameter θ) is plotted in figure 7(d). It is shown that this value is more than 1. The magnitude of θ increases with an increase of magnetic field and a decrease of pressure. The large values of θ and of radial pressure gradient should give a high separation factor, which indeed are confirmed in experiment.

The mass-spectrometer measurements were made at various radii in a midplane and at axis of the chamber (figure 1). It was found that the sample probe disturbed too much plasma at $r < 7 \text{ cm}$. We observed essential radial redistribution of plasma density under acceleration, accordingly the gas quantity q had been extracted by the valve. The value of q at $r = 10 \text{ cm}$ was ten times much as at $r = 0$. The radial density gradient increases with

ion velocity and temperature profiles in a plasma centrifuge

increasing molecular mass, magnetic field and discharge current. The magnitude of q at $B = 0.7 \text{ T}$ and $r = 0$ is smaller than that in the gas without the discharge. These results correlate well with spectroscopic measurements. The separation factors α for the 50% Ar–50% Kr and 50% Ar–50% Xe mixtures ($p_0 = 5 \text{ Pa}$, $B_0 = 0.7 \text{ T}$) are 14 ± 3 and 22 ± 4 at $r_1 = 7.5 \text{ cm}$ and $r_2 = 10.5 \text{ cm}$ respectively.

5. Conclusion

The probe and spectroscopic measurements in a highly ionized plasma centrifuge were performed. By means of an improved Abel inversion technique the radial ion velocity and temperature distribution have been calculated. Separation factors of 15 for Ar–Kr and 22 for Ar–Xe mixtures with density 10^{-21} m^{-3} are obtained. The velocity and temperature tomography equations can be used in other plasma devices.

Acknowledgment

This work was supported by the Technical Universities of Russia Foundation.

References

- [1] Belorusov A V, Karchevskii A I, Muromkin Yu A, Potanin E P, Ustinov A L and Babichev A P 1979 *Sov. J. Plasma Phys.* **5** 569
- [2] Wijnakker M M B and Granneman E H A 1980 *Z. Naturforsch.* **35A** 883
- [3] Prasad R R and Krishnan M 1987 *J. Appl. Phys.* **61** 4464
- [4] Geva M, Cohen C, Danziger O, Dothan F, Fridland L, Levin L A, Maharshak S and Hirshfield J L 1987 *IEEE Trans. Plasma Sci.* **15** 583
- [5] Efremov N P, Poluektov N P and Kharchenko V N 1995 *J. Quant. Spectrosc. Radiat. Transfer* **53** 723
- [6] Seraydarian R P, Burrell K H, Brooks N H, Groebner R J and Kan C 1986 *Rev. Sci. Instrum.* **57** 155
- [7] Mayo R M, Hurlburt D J and Fernandez J C 1993 *Phys. Fluids B* **5** 4002
- [8] Bohn W L, Beth M-U and Nedder G 1967 *J. Quant. Spectrosc. Radiat. Transfer* **7** 661
- [9] Lehnert B 1971 *Nucl. Fusion* **11** 485
- [10] Simpson S W 1975 *J. Phys. E: Sci. Instrum.* **8** 739
- [11] Deans S R 1983 *The Radon Transform and Some of its Applications* (New York: Wiley) p 282
- [12] Picalov V V and Preobrazhensky N G 1987 *Reconstructive Tomography in Gas Dynamic and Plasma Physics* (Novosibirsk: Nauka)
- [13] Lochte-Holtgreven W 1968 *Plasma Diagnostics* (Amsterdam: North-Holland)
- [14] Alfvén H 1954 *On the Origin of the Solar System* (Oxford: Oxford University Press)
- [15] Braginskii S I 1958 *Sov. Phys.-JETP* **6** 358
- [16] Kharchenko V N, Poluektov N P and Zverev V N 1990 *Exp. Therm. Fluid Sci.* **3** 567
- [17] James B W and Simpson S W 1976 *Plasma Phys.* **18** 289